Applied Physics B (2019)125:139
https://doi.org/10.1007/s00340-019-7249-1

Applied Physics B
Lasers and Optics

Second-harmonic wave patterns induced by the tightly focused radially polarized beam loaded with off-axis vortices

Jiehui Zhao[1,2] · Bowen Zhu[1] · Sixing Xi[3] · Quanquan Mu[2] · Shuai Wang[1] · Yuxin Dong[1] · Xiaolei Wang[1,2] · Zhuqing Zhu[4]

Received: 15 March 2019 / Accepted: 23 June 2019

Abstract
We investigated second-harmonic wave patterns induced by the tightly focused radially polarized beam loaded with off-axis vortices. The expression of the electric field of tightly focused radially polarized beam loaded with off-axis vortices through ZnSe crystal was derived, based on which the expression of the polarization distributions of near-field second-harmonic and the intensity distributions of far-field second-harmonic at different incident crystal planes were obtained. Numerical simulations indicated the distinctive polarization distributions of near-field second-harmonic and the intensity distributions of far-field second-harmonic when the incident crystal planes were (110) and (001). The results showed that second-harmonic wave patterns could be regulated flexibly by changing the distance and number of off-axis vortices.

1 Introduction

Second-harmonic generation (SHG) refers to the conversion of an incident optical field at frequency ω_0 to SH field at frequency $2\omega_0$ and arises from the second-order nonlinear optical susceptibility of the material [1–6]. SH imaging has been widely used in the fields of biomedicine, instrument science, and material analysis. For example, Moreaux et al. obtained a high-resolution optical imaging of cellular membranes and intact tissues by SHG microscopy [7, 8]. Shen used SHG and sum-frequency generation to monitor the surface dynamics of samples due to the nondestructive features of SH [9]. Cisek et al. used a noninvasive optical microscopy technique based on polarization-dependent SHG to determine the crystal lattice structure and microscopic heterogeneities within individual nanostructures [10–12].

Radially polarized beam (RPB) is a kind of spatially non-uniformly polarized beam and is attracting considerable attention owning to its unique properties [13–15]. RPB produces a strong longitudinal component when it is tightly focused. The focus spot size is smaller and the energy is more concentrated compared with linearly polarized beam under the same condition. In recent years, researchers have focused on the study of the SHG induced by tightly focused RPB in nonlinear crystals. Kozawa et al. used RPB inducing SH in a non-centrosymmetric ZnSe crystal, in which the existence of the longitudinal electric field of tightly focused RPB was confirmed by the change of intensity distributions of SH [16]. Then, Kozawa et al. demonstrated that the contribution of longitudinal electric field generated by focused radially polarized beam was clearly distinguished from that by azimuthally polarized beam, and the experimental demonstration of SH wave patterns induced by (001) ZnSe is reported [17]. Ohtsu et al. theoretically calculated the SH wave patterns induced by the tightly focused RPB, and a typical intensity pattern with figure of eight was observed [18]. Then, Ohtsu et al. calculated the polarization distributions of near-field SH and the intensity distributions of far-field SH induced by the tightly focused RPB loaded with coaxial vortices, and they proved that coaxial vortices with different topological charges affect the SH wave patterns [19]. However, these methods are only restricted to produce

✉ Xiaolei Wang
wangxiaolei@nankai.edu.cn

1 Institute of Modern Optics, College of Electronic Information and Optical Engineering, Nankai University, Tianjin 300350, China

2 State Key Laboratory of Applied Optics, Changchun Institute of Optics, Fine Mechanics and Physics, Chinese Academy of Sciences, Changchun 130033, Jilin, China

3 School of Science, Hebei University of Engineering, Handan 056038, Hebei, China

4 Key Laboratory of Optoelectronic Technology of Jiangsu Province, School of Physical Science and Technology, Nanjing Normal University, Nanjing 210023, Jiangsu, China

Published online: 02 July 2019

symmetric SH wave patterns. Generation of non-symmetric patterns or even arbitrary shaped patterns of SH wave to meet diverse demands from different aspects such as crystal lattice structure detection and optical imaging remains elusive. Since the existence of the off-axis vortex breaks the symmetrical distribution of the light field, it can effectively regulate the energy distribution of the focused field. A method of focusing the RPB loaded with multiple off-axis vortices on the ZnSe crystal can be applied to generate non-circularly symmetric SH wave patterns.

In this paper, SH wave patterns induced by the tightly focused RPB loaded with off-axis vortices are studied for the first time. The expression of the electric field of tightly focused RPB loaded with off-axis vortices through ZnSe crystal is derived firstly. Then, the expression of the polarization distributions of near-field SH and the intensity distributions of far-field SH are derived when the incident crystal planes are (110) and (001), respectively. In the numerical simulations, influence of the distance and number of off-axis vortices on near- and far-field SH wave patterns are analyzed. Finally, the rules of the SH wave patterns under the control of multiple off-axis vortices are explored. This work demonstrates that the distance and number of off-axis vortices could provide new degrees of freedom for SHG, making the manipulation of the SH wave patterns more flexible.

2 Theory

Figure 1 shows the schematic of SHG induced by the tightly focused RPB loaded with off-axis vortices. A linearly polarized Gaussian beam is converted to an RPB loaded with off-axis vortices through a spiral phase plate and a radial polarization converter. The RPB loaded with off-axis vortices is tightly focused in the ZnSe crystal by the high numerical aperture objective to generate SH. Near-field observation screen of SH wave patterns is located on the back surface of the ZnSe crystal (xOy plane), where $P(r, \varphi, 0)$ is the observation point. The far-field observation screen of SH wave patterns is located in the position of $z = z_d$ ($x_dO_dy_d$ plane), where $Q\left(R\sin\Theta, \Phi, Z_d\right)$ is the observation point.

2.1 The tightly focused field through ZnSe crystal

Assuming that the incident cylindrical vector beam conforms to the Gaussian distribution, the electric field of RPB can be expressed as follows:

$$\vec{E}_\rho = E_0 \exp\left(-\frac{\rho^2}{\omega^2}\right)\vec{e}_\rho = E_\rho \vec{e}_\rho \tag{1}$$

where ω is the waist radius of the incident Gaussian beam, (ρ, ϕ) is polar coordinate in the object space, where f is the focal length of the objective and $\vec{e}_\rho$ is the radial unit vector. Assuming that an off-axis vortex is located at the point P_1 in the object space and can be expressed as $\rho_1 e^{j\phi_1}$, so the incident field can be expressed as follows [20]:

$$\vec{E}_{in0}(\rho, \phi) = \vec{E}_\rho\left(\rho e^{j\phi} - \rho_1 e^{j\phi_1}\right)^{m_1} \tag{2}$$

where m_1 is the topological charge of the single vortex. When incident beam carries multiple off-axis vortices, whose locations are centered at $P_1, P_2, \ldots, P_N$ with topological charges are $m_1, m_2, \ldots, m_N$, respectively, the expression of incident field can be given as follows [20]:

$$\vec{E}_{in0}(\rho, \phi) = \vec{E}_\rho \sum_{i=0}^{M} A_n \rho^{M-i} e^{j(M-i)\phi} \tag{3}$$

where A_n is the coefficient of multiple vortices expansion, and $M = \sum_{n=1}^{N} m_n$. Based on Richards–Wolf vector diffraction theory [21], the components of electric field of tightly

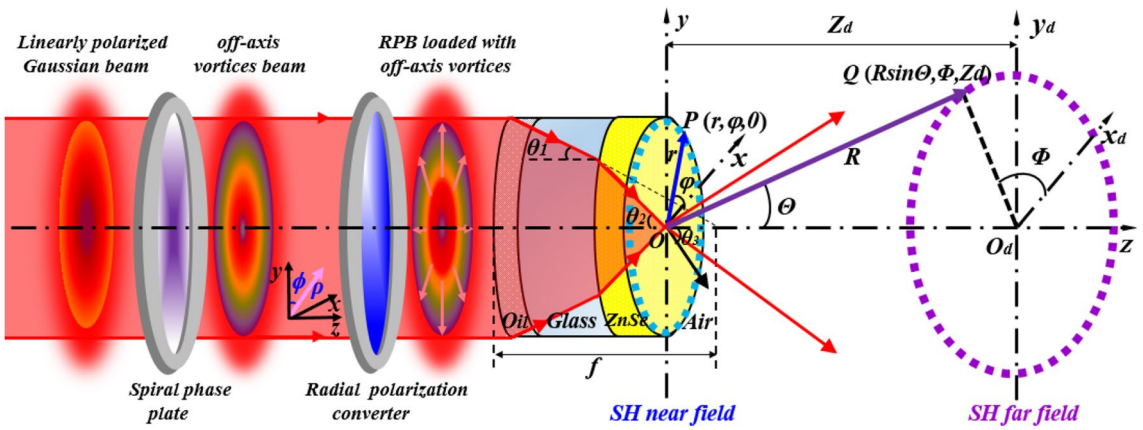

Fig. 1 Schematic of the SHG induced by the tightly focused RPB loaded with off-axis vortices

focused RPB loaded with multiple vortices can be expressed as follows [20]:

$$\vec{E}_{\text{in}}(r,\varphi,z)=\begin{pmatrix}E_{\text{in\_}r}\\E_{\text{in\_}\varphi}\\E_{\text{in\_}z}\end{pmatrix}=-\frac{fk}{2}\sum_{n=0}^{M}j^{l}A_n\exp(j(M-n)\varphi)\times\int_0^{\alpha}\vec{E}_{\rho}\rho^{M-n}\sqrt{\cos\theta}\sin\theta\exp(jkz\cos\theta)\times\begin{pmatrix}\cos\theta\left[J_{l+1}(kr\sin\theta)-J_{l-1}(kr\sin\theta)\right]\\-j\cos\theta\left[J_{l+1}(kr\sin\theta)+J_{l-1}(kr\sin\theta)\right]\\2j\sin\theta J_l(kr\sin\theta)\end{pmatrix}\mathrm{d}\theta \tag{4}$$

where α is the maximum angle related to the numerical aperture (NA) of the objective, $\alpha=\arcsin(\mathrm{NA}/n_1)$, and n_1 is the refractive index of objective. $J_l(kr\sin\theta)$ is the Bessel function of the first kind of order l, $l=M-n$. The components of electric field of tightly focused RPB through a dielectric surface in cylindrical coordinates can be expressed as follows [22]:

$$\vec{E}(r,\varphi,z)=-\frac{jfk_3}{2\pi}\int_0^{\alpha}\mathrm{d}\theta_1\int_0^{2\pi}\vec{E}_{\text{in}}\sqrt{\cos\theta_1}\left(\frac{k_3}{k_1}\right)\times\exp\left[-jd\left(k_1\cos\theta_1-k_3\cos\theta_3\right)\right]\times\begin{pmatrix}t^p\cos\theta_3\cos(\phi-\varphi)\\t^s\cos\theta_3\sin(\phi-\varphi)\\-t^p\sin\theta_3\end{pmatrix}\exp\left[j\left(k_3z\cos\theta_3+k_1r\sin\theta_1 cos(\varphi-\phi)\right)\right]\sin\theta_1\mathrm{d}\phi, \tag{5}$$

where $k_1=\frac{2\pi n_1}{\lambda}$ is the wavenumber in the objective, $k_3=\frac{2\pi n_3}{\lambda}$ is the wavenumber in free space, λ is the wavelength of incident beam, and n_3 is the refractive index of air. The electric field components of tightly focused RPB loaded with multiple vortices through ZnSe crystal in the xOy plane can be obtained by substituting Eqs. (4)–(5), there are as follows:

$$\vec{E}(r,\varphi,z)=\begin{pmatrix}E_r\\E_{\varphi}\\E_z\end{pmatrix}=-\frac{fk_3}{2}\sum_{n=0}^{M}j^{l}A_n\exp\left[j(M-n)\varphi\right]\times\int_0^{\alpha}\vec{E}_{\rho}\rho^{M-n}\left(\frac{k_3}{k_1}\right)\sqrt{\cos\theta_1}\sin\theta_1\times\exp\left[-jd\left(k_1\cos\theta_1-k_3\cos\theta_3\right)\right]\exp(jk_3z\cos\theta_3)\times\begin{pmatrix}t^p\cos\theta_3\left[J_{l+1}(k_1r\sin\theta_1)-J_{l-1}(k_1r\sin\theta_1)\right]\\-jt^s\cos\theta_3\left[J_{l+1}(k_1r\sin\theta_1)+J_{l-1}(k_1r\sin\theta_1)\right]\\-2jt^p\sin\theta_3J_l(k_1r\sin\theta_1)\end{pmatrix}\mathrm{d}\theta_1 \tag{6}$$

where $\theta_2=\arcsin\left(n_1\sin\theta_1/n_2\right)$, $\theta_3=\arcsin\left(n_1\sin\theta_1/n_3\right)$, and t^s and t^p are the amplitude transmission factors for polarization states parallel and perpendicular to the surface of glass-ZnSe, respectively, $t^s=\frac{2\sin\theta_2\cos\theta_1}{\sin\left(\theta_1+\theta_2\right)}$, $t^p=\frac{2\sin\theta_2\cos\theta_1}{\sin\left(\theta_1+\theta_2\right)\cos\left(\theta_1-\theta_2\right)}$.

2.2 Calculation of near-field SH wave patterns

The SH wave patterns induced in the (110) and (001) crystal planes of the ZnSe crystal are investigated, respectively. Figure 2 shows the relationship between the crystal axes of the (110) and (001) crystal planes and Cartesian coordinate axes. x', y', z' denote crystal axes, and x, y, z denote Cartesian coordinate axes.

The second-order nonlinear polarization intensity components of a ZnSe crystal can be expressed as follows [19]:

$$\begin{pmatrix}P_{x'}^{(2\omega)}\\P_{y'}^{(2\omega)}\\P_{z'}^{(2\omega)}\end{pmatrix}=\begin{pmatrix}0&0&0&d&0&0\\0&0&0&0&d&0\\0&0&0&0&0&d\end{pmatrix}\begin{pmatrix}(E_{x'}^{(\omega)})^2\\(E_{y'}^{(\omega)})^2\\(E_{z'}^{(\omega)})^2\\2E_{y'}^{(\omega)}E_{z'}^{(\omega)}\\2E_{z'}^{(\omega)}E_{x'}^{(\omega)}\\2E_{x'}^{(\omega)}E_{y'}^{(\omega)}\end{pmatrix} \tag{7}$$

where d is the component of nonlinear susceptibility tensor, $E_{i'}^{(\omega)}$ is the electric field component of the incident fundamental beam, and $P_{i'}^{(2\omega)}$ is nonlinear polarization of SH in the crystal axis coordinates. Since crystal axes are inconsistent with Cartesian coordinate axes in the (110) crystal plane, the electric field components of the incident fundamental beam in crystal axis coordinates are projected to the Cartesian coordinates and can be expressed as follows:

$$\begin{cases}E_x=-E_{z'}\\E_y=E_{x'}\sin45^{\circ}-E_{y'}\cos45^{\circ}\\E_z=-E_{x'}\cos45^{\circ}-E_{y'}\sin45^{\circ}\end{cases} \tag{8}$$

Thus, the nonlinear polarization of near-field SH in the Cartesian coordinates can be expressed as follows:

$$\vec{P}_{(110)}^{(2\omega)}=\begin{pmatrix}P_x^{(2\omega)}\\P_y^{(2\omega)}\\P_z^{(2\omega)}\end{pmatrix}=d\begin{pmatrix}(E_y^{(\omega)})^2-(E_z^{(\omega)})^2\\2E_x^{(\omega)}E_y^{(\omega)}\\-2E_z^{(\omega)}E_x^{(\omega)}\end{pmatrix} \tag{9}$$

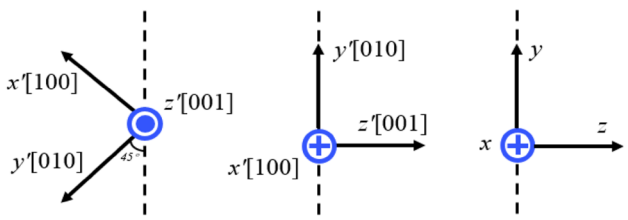

Fig. 2 Schematic of the crystal coordinate axes of the (110) and (001) crystal planes and Cartesian coordinate axes

The Cartesian coordinates and cylindrical coordinates have the following transformations:

$$\begin{cases} E_x = E_r \cos\varphi - E_\varphi \sin\varphi \\ E_y = E_r \sin\varphi + E_\varphi \cos\varphi \\ E_z = E_z \end{cases} \tag{10}$$

For the convenience of calculation, the nonlinear polarization of near-field SH can be obtained by substituting Eqs. (10) into (9), there are as follows:

$$\begin{pmatrix} P^{(2\omega)}_{x(110)} \\ P^{(2\omega)}_{y(110)} \\ P^{(2\omega)}_{z(110)} \end{pmatrix} = d \begin{pmatrix} (\sin\varphi)^2 (E_r^{(\omega)})^2 + (\cos\varphi)^2 (E_\varphi^{(\omega)})^2 + 2E_r^{(\omega)} E_\varphi^{(\omega)} \sin\varphi\cos\varphi - (E_z^{(\omega)})^2 \\ 2\sin\varphi\cos\varphi (E_r^{(\omega)})^2 - 2\sin\varphi\cos\varphi (E_\varphi^{(\omega)})^2 + 2\left[(\cos\varphi)^2 - (\sin\varphi)^2\right] E_r^{(\omega)} E_\varphi^{(\omega)} \\ -2\cos\varphi E_z^{(\omega)} E_r^{(\omega)} + 2\sin\varphi E_z^{(\omega)} E_\varphi^{(\omega)} \end{pmatrix} \tag{11}$$

where E_r, E_φ, and E_z in the Eq. (11) can be obtained by Eq. (6).

When the incident crystal plane is (001), crystal axes are consistent with the Cartesian coordinate axes, so there are as follows:

$$\vec{P}^{(2\omega)}_{(001)} = \begin{pmatrix} P_x^{(2\omega)} \\ P_y^{(2\omega)} \\ P_z^{(2\omega)} \end{pmatrix} = 2d \begin{pmatrix} E_y^{(\omega)} E_z^{(\omega)} \\ E_z^{(\omega)} E_x^{(\omega)} \\ E_x^{(\omega)} E_y^{(\omega)} \end{pmatrix} \tag{12}$$

The nonlinear polarization of near-field SH in the xOy plane can be obtained by the following:

$$\begin{pmatrix} P^{(2\omega)}_{x(001)} \\ P^{(2\omega)}_{y(001)} \\ P^{(2\omega)}_{z(001)} \end{pmatrix} = 2d \begin{pmatrix} \sin\varphi E_z^{(\omega)} E_r^{(\omega)} + \cos\varphi E_z^{(\omega)} E_\varphi^{(\omega)} \\ \cos\varphi E_z^{(\omega)} E_r^{(\omega)} - \sin\varphi E_z^{(\omega)} E_\varphi^{(\omega)} \\ \sin\varphi\cos\varphi (E_r^{(\omega)})^2 - \sin\varphi\cos\varphi (E_\varphi^{(\omega)})^2 + \left[(\cos\varphi)^2 - (\sin\varphi)^2\right] E_r^{(\omega)} E_\varphi^{(\omega)} \end{pmatrix} \tag{13}$$

Similarly, E_r, E_φ, and E_z in Eq. (13) can be obtained by Eq. (6).

2.3 Calculation of far-field SH wa ve patterns

Green's function approach is applied to calculate the far-field SH wave patterns in the $x_d O_d y_d$ plane [18], and the components of electric field of far-field SH can be expressed as follows:

$$\begin{pmatrix} E_r^{(2\omega)} \\ E_\varphi^{(2\omega)} \\ E_z^{(2\omega)} \end{pmatrix} = -\frac{\omega_{SH}^2}{c^2} \frac{\exp(jk_{SH}|\vec{R}|)}{|\vec{R}|} \iiint \exp\left[\frac{jk_{SH}\vec{r}\cdot\vec{R}}{|\vec{R}|}\right] B\vec{P}^{(2\omega)}(\vec{r}) dV \tag{14}$$

where $B = \begin{pmatrix} 0 & 0 & 0 \\ \sin\Theta\cos\Phi & \cos\Theta\sin\Phi & -\sin\Theta \\ -\sin\Phi & \cos\Phi & 0 \end{pmatrix} \circ k_{SH}$ and ω_{SH} (is equal to $2\omega_0$) are the wave number and frequency of the SH wave, respectively. V is the volume of the ZnSe crystal sample. $\vec{r}$ and $\vec{P}^{(2\omega)}(\vec{r})$ are the displacement vector (the blue arrow in Fig. 1) and the nonlinear polarization intensity vector of near-field observation point from the point O, respectively. $\vec{R}$, Θ and Φ are the displacement vector (the purple arrow in Fig. 1), polar angle, and azimuthal angle of the far-field observation point from point O, respectively. Assuming that the ZnSe crystal is infinitely thin, the volume integral can be simplified to surface integral. Using the fast Fourier transform algorithm, the components of electric field of far-field SH can be obtained easily by the following:

$$\begin{aligned} \begin{pmatrix} E_r^{(2\omega)} \\ E_\varphi^{(2\omega)} \\ E_z^{(2\omega)} \end{pmatrix} &= -\frac{\omega_{SH}^2}{c^2} \frac{\exp(jk_{SH}|\vec{R}|)}{|\vec{R}|} \iint \exp\left[\frac{-jk_{SH}\vec{r}\cdot\vec{R}}{|\vec{R}|}\right] B\vec{P}^{(2\omega)}(\vec{r}) dS \\ &= -2\pi \frac{\omega_{SH}^2}{c^2} \frac{\exp(jk_{SH}|\vec{R}|)}{|\vec{R}|} B^* \begin{pmatrix} \mathrm{FFT}\left[P_x^{(2\omega)}(\vec{r})\right] \\ \mathrm{FFT}\left[P_y^{(2\omega)}(\vec{r})\right] \\ \mathrm{FFT}\left[P_z^{(2\omega)}(\vec{r})\right] \end{pmatrix} \end{aligned} \tag{15}$$

where $B^* = \begin{pmatrix} \cos^2\Theta\cos\Phi & -\sin\Phi & -\sin\Theta\cos\Theta\cos\Phi \\ \cos^2\Theta\sin\Phi & \cos\Phi & -\sin\Theta\cos\Theta\sin\Phi \\ \sin\Theta\cos\Theta & 0 & \sin^2\Theta \end{pmatrix}$.

When the incident crystal plane is (110), the electric field intensity components of far-field SH in the $x_d O_d y_d$ plane can be obtained by substituting Eq. (11) into Eq. (15). When the incident crystal plane is (001), the electric field intensity components of far-field SH in the $x_d O_d y_d$ plane can be obtained by substituting Eq. (13) into Eq. (15).

3 The SH wave patterns

The off-axis optical vortices could generate distinctive intensity, phase, and polarization distributions to the incident beam due to the particular helical phase structures and central singularities, resulting in a change in the proportion of polarization components of the SH wave patterns. Therefore, the SH wave patterns induced by the RPB loaded with off-axis vortices are different from the case that beam are loaded with coaxial vortex or non-vortex. In this case, the influence of the distance and number of off-axis on near- and far-field SH wave patterns are analyzed when the incident crystal planes are (110) and (001). In the numerical simulations, the parameters are chosen as follows: the wavelength of incident beam is $\lambda = 1200$ nm, the waist radius of Gaussian beam is $\omega = 2.56$ mm, the refractive index of objective is $n_1 = n_{\text{oil}} = n_{\text{glass}} = 1.515$, the numerical aperture of objective is NA = 1.2, the refractive index of ZnSe crystal is $n_2 = 2.472$, the refractive index of air is $n_3 = 1$, and the distance between xOy plane and $x_dO_dy_d$ plane is $z_d = 20\lambda$.

3.1 Influence of the distance of single off-axis vortex on SH wave patterns

When the distance from single off-axis vortex to the origin of the coordinate axis (l_v) is changed, the SH wave patterns in the (110) crystal plane are shown in Fig. 3, in which the topological charge of single vortex is chosen as $m = 1$. When single coaxial vortex exists in the center of incident field, total near- and far-field SH wave patterns are both central bright spots with weak lobes, which are symmetrical about Cartesian coordinate axes. When single

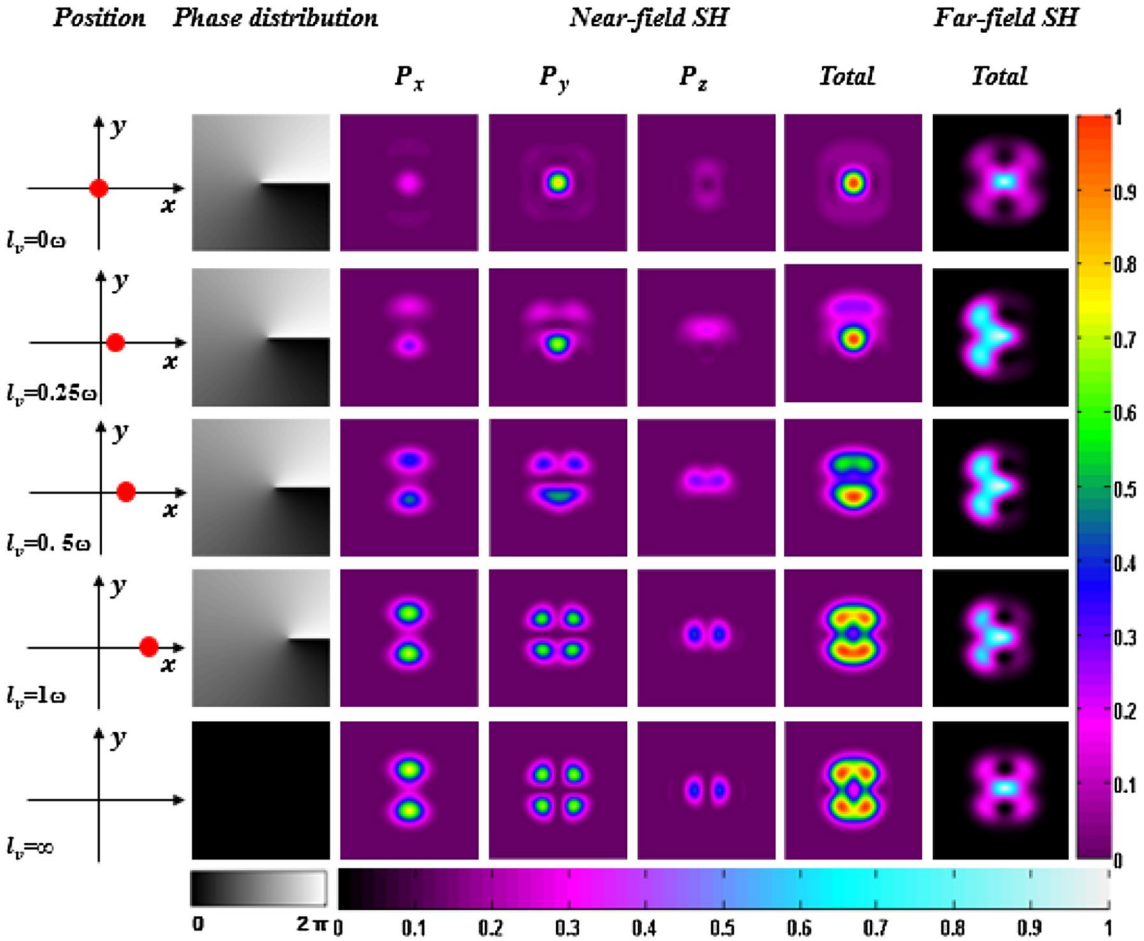

Fig. 3 The SH wave patterns induced by tightly focused RPB in the (110) crystal plane of the ZnSe crystal when the distance of the single off-axis vortex is changed. The first column is the distance and position of single off-axis vortex. The second column shows the phase distribution of single off-axis vortex. The third-to-sixth columns are the polarization distributions of SH wave in near field which are P_x component, P_y component, P_z component, and total field, respectively. The imaging area is $2\lambda \times 2\lambda$ and the colorbar is displayed on the right side of the image. The seventh column is the intensity distributions of SH wave in far field, in which the imaging area is $15\lambda \times 15\lambda$ and the colorbar is displayed below the image

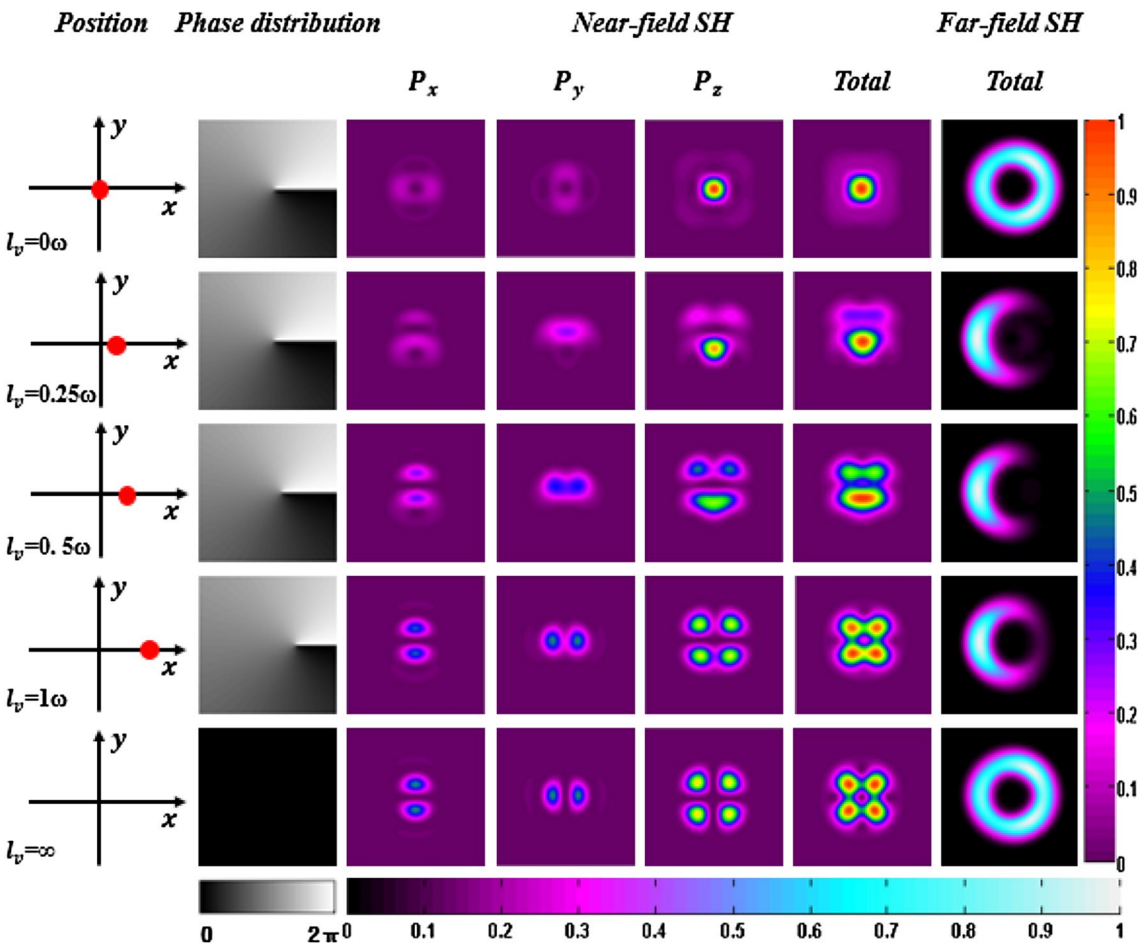

Fig. 4 The SH wave patterns induced by tightly focused RPB in the (001) crystal plane of the ZnSe crystal when the distance of the single off-axis vortex is changed. The layout of figure and colorbar is the same as in Fig. 3

off-axis vortex exists in the incident field, the energy of focused field tends to the one side without vortex, which breaks the symmetry of near- and far-field SH wave patterns. In the range of $l_v < \omega$, with the increase of the distance of single off-axis vortex, P_x component is gradually transformed from a three-lobe pattern whose the middle part is stronger and the edges are weaker to a two-lobe pattern along the y axis. P_y component is gradually transformed from a strong circular spot to a four-peak pattern. P_z component is transformed from a single hollow spot to two-lobe pattern along the x axis. P_x and P_y components account for a large proportion of polarization distributions of near-field SH. Compared with the case that beam are loaded with single coaxial vortex, total far-field SH wave patterns are concentrated on the side of $x < 0$, which present asymmetrical distributions along the x axis. In the range of $l_v > \omega$, the single off-axis vortex has less and less effect on the focused field and generated SH wave patterns. When l_v approaches to infinity, total far-field SH wave pattern is an eight-figure shape, and the existence of single off-axis vortex almost has no effect on far-field SH wave patterns, the far-field SH wave patterns are approximately equal to the case without vortex.

When the distance of single off-axis vortex is changed, the SH wave patterns in the (001) crystal plane are shown in Fig. 4. When single coaxial vortex exists in the center of the incident field, total near-field SH wave pattern is a central bright spot which is symmetrical about Cartesian coordinate axes. Total far-field SH wave pattern is a bright ring of circle. When single off-axis vortex exists in the incident field, in the range of $l_v < \omega$, with the increase of the distance of single off-axis vortex, P_x and P_y components are gradually transformed from a light spot to a two-lobe pattern which are vertically and horizontally symmetrical, respectively. P_z component is gradually transformed from a strong circular spot to a four-peak pattern. Different with the case of (110) crystal plane, P_z component is dominant in the polarization distributions of near-field SH, and total near-field SH wave patterns are the half of moon shapes on the side of $x < 0$. There is a phase singularity in the center of a single

off-axis vortex, which breaks the energy symmetry of the focused field and leads the energy to the side of non-vortex. With the increase of l_v, the near- and far-field SH wave patterns induced by the tightly focused RPB loaded with single off-axis vortex tend to be symmetrical. l_v will contribute to the asymmetrically distributed focused field when it takes a finite value.

3.2 Influence of the number of off-axis vortices on SH wave patterns

When the number of multiple off-axis vortices is changed, the SH wave patterns in the (110) crystal plane are shown in Fig. 5, in which the distance of off-axis is chosen as $l_v = 0.5\omega$. When there is no vortex in the incident field, near-and far-field SH wave patterns are both symmetrical about Cartesian coordinate axes. As the number of off-axis vortices increases, P_x component exhibits a vertically symmetrical spot, while the symmetry of P_y component, P_z component, and total near- and far-field SH wave patterns are broken. Besides, P_x and P_y components account for a large proportion of polarization distributions of near-field SH. The center of far-field SH wave patterns is bright and the surroundings are dark. Due to the existence of a phase singularity at the center of vortex, the energy of focused field will be taken to the side of non-vortex. When there are multiple off-axis vortices in the incident light field, the SH wave patterns will be the result of a superposition of the influence of single off-axis vortex on the light field.

When the number of multiple off-axis vortices is changed, the SH wave patterns in the (001) crystal plane are shown in Fig. 6, which indicates that P_z component is dominant in the polarization distributions of near-field SH. Different with the condition of (110) crystal plane, the center of the far-field

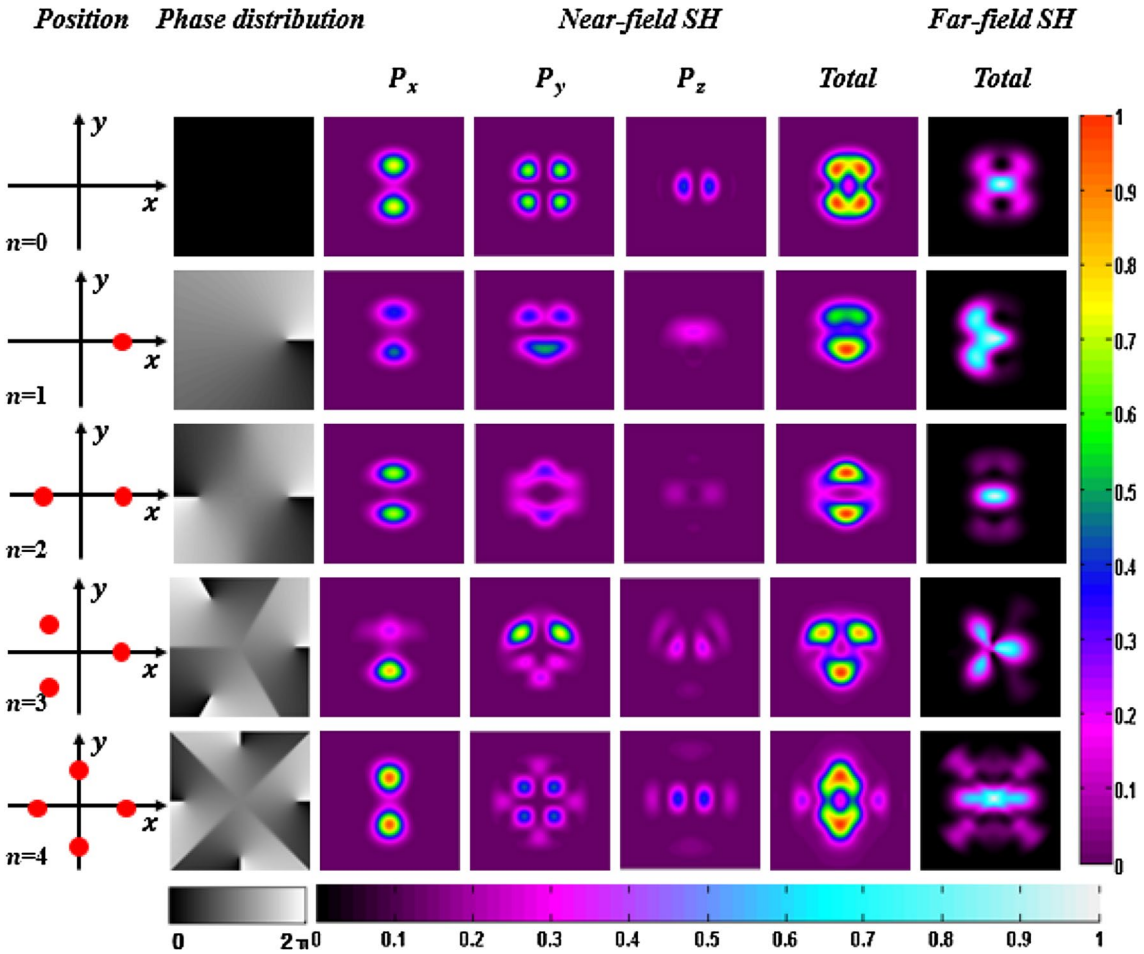

Fig. 5 The SH wave patterns induced by tightly focused RPB in the (110) crystal plane of the ZnSe crystal when the number of the multiple off-axis vortices is changed. The first column is the number and position of multiple off-axis vortices. The second column shows the phase distribution of multiple off-axis vortices. The third-to-sixth columns are the polarization distributions of SH wave in near-field which are P_x component, P_y component, P_z component, and total field, respectively. The imaging area is $2\lambda \times 2\lambda$ and the colorbar is displayed on the right side of the image. The seventh column is the intensity distributions of SH wave in far field, in which the imaging area is $15\lambda \times 15\lambda$ and the colorbar is displayed below the image

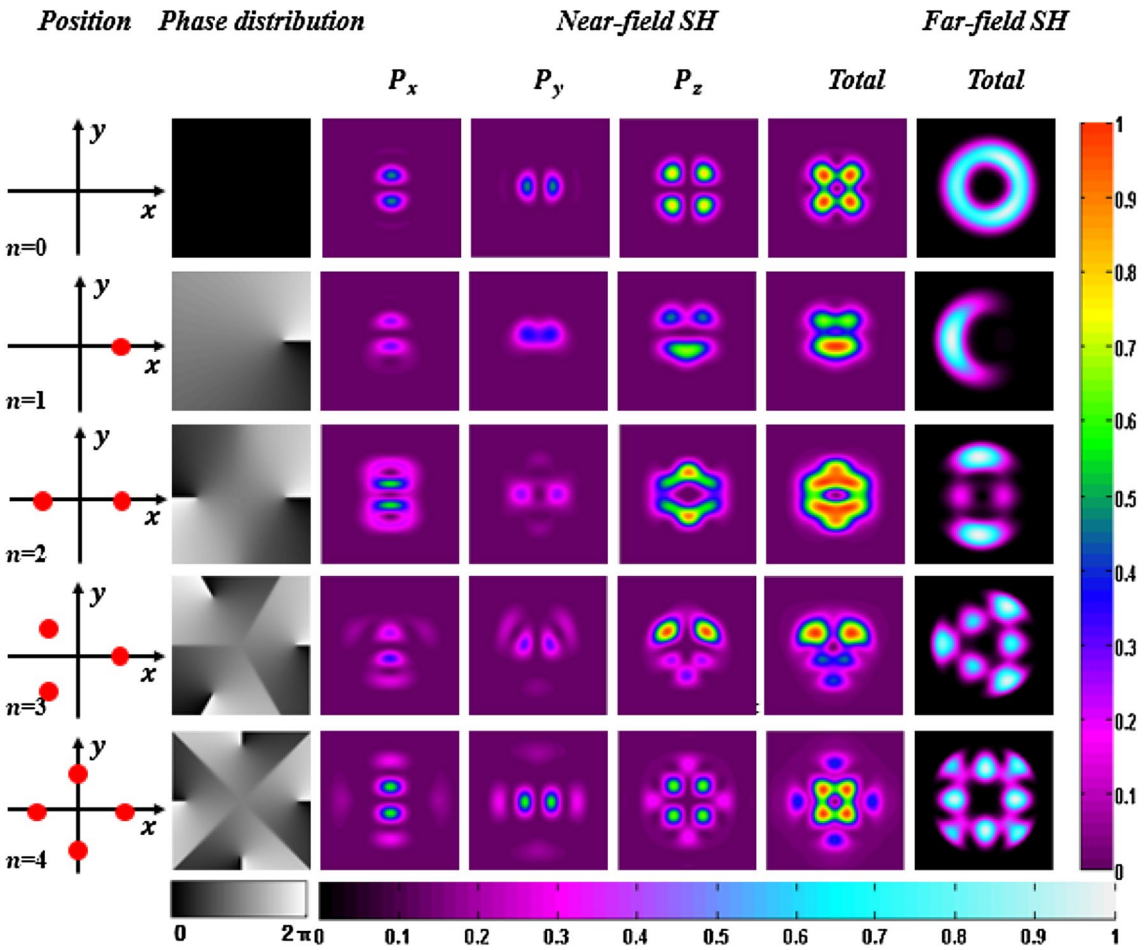

Fig. 6 The SH wave patterns induced by tightly focused RPB in the (001) crystal plane of the ZnSe crystal when the number of the multiple off-axis vortices is changed. The layout of figure and colorbar is the same as in Fig. 3

SH wave patterns is dark and surroundings are bright. With the increase of the number of off-axis vortices, the far-field SH wave patterns become to polygons, and the number of edges of the polygons is equal to the number of off-axis vortices. In other words, the far-field SH wave patterns follow the arrangement of multiple off-axis vortices.

4 Conclusion

We studied the characteristics of the SH wave patterns induced by tightly focused RPB loaded with single off-axis vortex and multiple off-axis vortices. The results showed that the distance and number of the off-axis vortices would affect SH wave patterns. (1) When the number of off-axis vortices was a constant and the distance of off-axis vortices was in the range of $0 < l_v < \omega$, the SH wave patterns was changed clearly with l_v. The existence of a phase singularity at the center of vortex drove the focused field to the side of non-vortex. (2) When the distance of off-axis vortices was constant, with the increase of the number of off-axis vortices, the SH wave patterns presented asymmetrical distributions and became more and more diverse. The SH wave patterns were the result of a superposition of the influence of the single off-axis vortex on the focused field. (3) Different crystal planes show different SH wave patterns. When the crystal plane was (110), the P_x and P_y components were dominant in the polarization distributions of near-field SH, while the P_z was dominant when the crystal plane is (001). The results demonstrated that SH wave patterns could be effectively manipulated by changing the distance and number of off-axis vortices, which provided a new method to determine crystal axis and analyze the type of the crystal material.

Funding This study was funded by National Natural Science Foundation of China (NSFC) (Grant Number 61875093) and the State Key Laboratory of Applied Optics.

Compliance with ethical standards

Conflict of interest The authors declare that they have no conflict of interest.

References

1. J. Martorell, R. Vilaseca, R. Corbalán, Appl. Phys. Lett. **70**, 702 (1997)
2. H. Cao, J.Y. Wu, H.C. Ong, J.Y. Dai, R.P.H. Chang, Appl. Phys. Lett. **73**, 572 (1998)
3. G. Bautista, M.J. Huttunen, J. Mäkitalo, J.M. Kontio, J. Simonen, M. Kauranen, Nano Lett. **12**, 3207 (2012)
4. B. Metzger, L. Gui, J. Fuchs, D. Floess, M. Hentschel, H. Giessen, Nano Lett. **15**, 3917 (2015)
5. S. Kruk, R. Camacho-Morales, L. Xu, M. Rahmani, A. Smirnova, L. Wang, H. Tan, C. Jagadish, N. Neshev, S. Kivshar, Nano Lett. **17**, 3914 (2017)
6. Daria Smirnova, Alexander I. Smirnov, Yuri S. Kivshar, Phys. Rev. A **97**, 013807 (2018)
7. L. Moreaux, O. Sandre, J. Mertz, J. Opt. Soc. Am. B **17**, 1685 (2000)
8. P.J. Campagnola, H.A. Clark, W.A. Mohler, A. Lewis, L.M. Loew, J. Biomed. Opt. **6**, 277 (2001)
9. Y.R. Shen, Nature **337**, 519 (1989)
10. R. Cisek, D. Tokarz, N. Hirmiz, A. Saxena, A. Shik, H.E. Ruda, V. Barzda, Nanotechnology **25**, 505703 (2014)
11. B. Ruiz, Z. Yang, V. Gramlich, M. Jazbinsek, P. Günter, J. Mater. Chem. **16**, 2839 (2006)
12. N. Ennaceur, I. Ledoux-Rak, J. Phys. Chem. Solids **120**, 223 (2018)
13. T. Bauer, S. Orlov, U. Peschel, P. Banzer, G. Leuchs, Nat. Photon. **8**, 23 (2013)
14. S.N. Khonina, I. Golub, J. Opt. Soc. Am. A **33**, 1948 (2016)
15. Y. Kozawa, S. Sato, Opt. Express **18**, 10828 (2010)
16. Y. Kozawa, S. Sato, J. Opt. Soc. Am. B **25**, 175 (2008)
17. Y. Kozawa, A. Ohtsu, S. Sato, in Advanced Solid-State Photonics, (Optical Society of America, 2010), paper AMB28
18. A. Ohtsu, Y. Kozawa, S. Sato, Appl. Phys. B **98**, 851 (2010)
19. A. Ohtsu, Opt. Commun. **283**, 3831 (2010)
20. X. Wang, B. Zhu, Y. Dong, S. Wang, Z. Zhu, F. Bo, X. Li, Opt. Express **25**, 26844 (2017)
21. B. Richards, E. Wolf, Proc. R. Soc. Lond. A Math. Phys. Sci. **253**, 358 (1959)
22. D.P. Biss, T.G. Brown, Opt. Express **9**, 490 (2001)